Enhanced Mobility-Lifetime Products in PbS Colloidal Quantum Dot Photovoltaics

Kwang S. Jeong,[†] Jiang Tang,[‡] Huan Liu,[‡,§] Jihye Kim,[†] Andrew W. Schaefer,[†] Kyle Kemp,[‡] Larissa Levina,[‡] Xihua Wang,[‡] Sjoerd Hoogland,[‡] Ratan Debnath,[‡] Lukasz Brzozowski,[‡] Edward H. Sargent,[‡] and John B. Asbury[†,*]

[†]Department of Chemistry, The Pennsylvania State University, University Park, Pennsylvania 16802, United States, [‡]Department of Electrical and Computer Engineering, University of Toronto, 10 King's College Road, Toronto, Ontario M5S 3G4, Canada, and [§]Department of Electronic Science and Technology, Huazhong University of Science and Technology, Wuhan, 430074, People's Republic of China

ABSTRACT

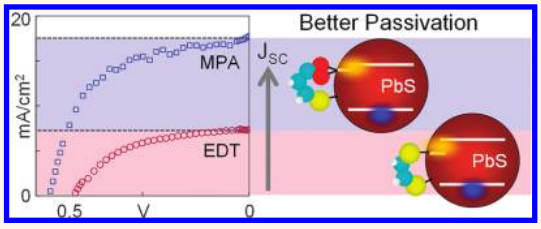

Colloidal quantum dot (CQD) photovoltaics offer a promising approach to harvest the near-IR region of the solar spectrum, where half of the sun's power reaching the earth resides. High external quantum efficiencies have been obtained in the visible region in lead chalcogenide CQD photovoltaics. However, the corresponding efficiencies for band gap radiation in the near-infrared lag behind because the thickness of CQD photovoltaic layers from which charge carriers can be extracted is limited by short carrier diffusion lengths. Here, we investigate, using a combination of electrical and optical characterization techniques, ligand passivation strategies aimed at tuning the density and energetic distribution of charge trap states at PbS nanocrystal surfaces. Electrical and optical measurements reveal a more than 7-fold enhancement of the mobility-lifetime product of PbS CQD films treated with 3-mercaptopropionic acid (MPA) in comparison to traditional organic passivation strategies that have been examined in the literature. We show by direct head-to-head comparison that the greater mobility-lifetime products of MPA-treated devices enable markedly greater short-circuit current and higher power conversion efficiency under AM1.5 illumination. Our findings highlight the importance of selecting ligand treatment strategies capable of passivating a diversity of surface states to enable shallower and lower density trap distributions for better transport and more efficient CQD solar cells.

KEYWORDS: colloidal quantum dot · photovoltaics · mobility-lifetime products · charge trapping · time-resolved infrared spectroscopy

Nearly half of the energy from the sun lies in the near-infrared (near-IR) region of the electromagnetic spectrum. Crystalline silicon solar cells have achieved 25%[1] power conversion efficiency in part because the low band gap of silicon enables these devices to efficiently utilize much of the solar energy in the near-IR region—but at a high energetic and economic cost. Efficient utilization of the near-IR region of the solar spectrum remains elusive for inexpensive alternatives to silicon solar cells such as amorphous silicon, dye-sensitized or organic thin film solar cells. Colloidal quantum dot (CQD) photovoltaics represent a unique pathway to high efficiency solar cells because they are potentially inexpensive and offer size-tunability, enabling multijunction cells but with the simplicity of uniform chemistry and processing conditions.[2,3]

Rapid advances in power conversion efficiency of CQD photovoltaics have occurred in recent years. The first types of test structures with efficiencies greater than 1% utilized a Schottky junction to generate a depletion layer between p-type PbS,[4−7] PbSe,[8] or ternary PbS_xSe_{1-x}[9] CQD films and low work function metal contacts such as aluminum or calcium. Charge collection in the photovoltaic active layers was most efficient in the depletion layer. Consequently, the optimal thickness of the active layer was determined to be close to the depletion width with corresponding power conversion efficiencies varying between 1.8 and 3.6% depending on the exact implementation. Subsequently, a depleted heterojunction architecture was utilized consisting of a p-type CQD film in contact with an n-type wide band gap semiconductor such as TiO_2 or ZnO.[10−15] The depleted heterojunction architecture overcame limitations of Schottky test structures by permitting somewhat thicker active layers and moving the depletion layer to the front contact to suppress recombination losses, resulting in power conversion efficiencies as high as 5.1%.[10] Yet, maximum reported EQE values for band gap excitation of planar PbS CQD test structures remain below 30% because charge collection is most efficient in

* Address correspondence to jasbury@psu.edu.

Received for review July 15, 2011 and accepted December 14, 2011.

Published online December 14, 2011
10.1021/nn2039164

the depletion layer, again prompting the thickness of optimized test structures to be similar to the width of the depletion layer.[6,8,16−18]

The power conversion efficiency of CQD photovoltaics is determined in part by the efficiency at which photons are absorbed and converted into independently diffusing charge carriers and by the quantum yield for collecting those charge carriers in an external circuit.[2,19] Optimized test structures must balance competing demands of these processes because each is optimized under different conditions. For example, an active layer thickness of 1 μm is required to absorb 90% of incident photons at the band gap of CQDs (ignoring reflection losses and with an absorption coefficient at the band gap of 10^4 cm^{-1}).[2] On the other hand, charge collection efficiency decreases as the active layer increases in thickness because charge carriers are susceptible to recombination if their transit time exceeds the charge recombination lifetime. This competition between electrical transport and charge recombination sets an effective electrical length of a few hundred nanometers in current optimized devices. The need to balance these processes makes it challenging to construct CQD test structures that absorb all incident photons, especially those in the near-IR close to the band gap. Nanostructured interfaces,[18,20] nanowires,[21] and hyperbranched[22] structures have been proposed as pathways to navigate the competing demands of efficient light absorption and charge collection.

A promising approach to increase the external quantum efficiency particularly at the band gap of PbS CQD films is to enhance the diffusion length of charge carriers so that charges can be harvested from thicker photovoltaic active layers.[2] The diffusion length, l, of charge carriers is related to the square root of the mobility-lifetime product, $\mu\tau$, according to

$$l = \sqrt{\frac{k_B T}{e}\mu\tau} \qquad (1)$$

where k_B, T, and e are Boltzmann's constant, temperature, and the elementary charge. We recently demonstrated enhancement in CQD power conversion efficiency to 5.1% under AM1.5 illumination using a novel ligand strategy based on 3-mercaptopropionic acid (MPA) that passivates metal PbS nanocrystal surfaces.[10]

Herein, we show that the superior photovoltaic performance of MPA-treated PbS CQD devices is a direct result of improved passivation with this ligand strategy leading to greater mobility-lifetime products and enhanced minority carrier transport. Analysis of defects and charge recombination dynamics using time-resolved infrared (TRIR) spectroscopy coupled with electrical measurements of minority carrier mobility reveals that the MPA ligand treatment strategy significantly reduces the density and energetic distribution of defects below the conduction band in comparison to ethane dithiol (EDT)-treated devices. The reduction in defect density coupled with greater mobility results in superior minority carrier transport in MPA-treated CQD films. We show by direct head-to-head comparison of CQD devices processed under identical conditions and with identical architectures that improved transport in MPA-treated CQD devices translates to markedly higher short-circuit current and power conversion efficiency in comparison to EDT-treated devices. The comparison of MPA and EDT treatment strategies reveals that it is the ability of MPA to present two types of functional groups, both thiols and carboxylate groups, to CQD surfaces that enables superior passivation for lower defect densities and energetic distributions. Our findings highlight the importance of ligand strategies that provide chemical diversity to passivate a variety of surface states combined with strong interparticle coupling to enable improved transport and higher power conversion efficiency in CQD photovoltaic devices.

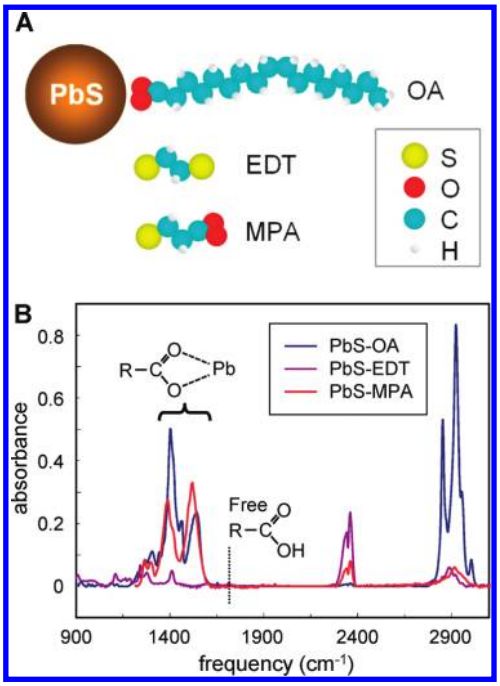

Figure 1. (A) Structures of ligands used to passivate 3.7 nm PbS CQD surfaces that are examined in this study: oleic acid (OA), ethanedithiol (EDT), and 3-mercaptopropionic acid (MPA). (B) Infrared spectra of films treated with various ligand strategies. The loss of carboxylate absorptions at 1400−1550 cm^{-1} in EDT-treated films demonstrate efficient removal of OA from PbS surfaces. The loss of CH stretching vibrations at 2900 cm^{-1} in MPA-treated films also indicates efficient removal of OA. The absence of an absorption peak at 1700 cm^{-1} indicates that all carboxylate groups are bonded to PbS surfaces.

RESULTS

PbS CQD films passivated by the original oleic acid (OA) ligands used during synthesis exhibit extremely low mobility as a result of the insulating nature of the long alkyl chains.[23] To make high mobility solids, it is

necessary to replace the original ligands with shorter molecules that increase the electronic coupling between neighboring nanocrystals.[19] Several ligand exchange strategies have been explored in the literature that include replacement of the original ligands with ethanedithiol,[5,8,11−13] benzenedithiol,[9,15,17] hydrazine,[23,24] and pyridine,[25] among others.[6,10,16,26−29] These ligand exchange treatments have led to impressive enhancements of carrier mobilities.[23,24,26,27] To explore the impact of various ligands on mobility-lifetime products in PbS CQD films, we examined solid state ligand exchange procedures utilizing EDT[5] and MPA[10] treatments of nominally 3.7 ± 0.18 nm PbS quantum dots. The size distribution of quantum dots was determined from the half-widths at half-maxima of the exciton absorption peaks in near-IR spectra of the dots in octane solution. The detailed analysis procedures are described in Supporting Information. Structures of these ligands are represented in Figure 1A. Top view SEM images of CQD films fabricated using eight successive layer-by-layer ligand exchange treatments with EDT and MPA are represented in Figure S2 (Supporting Information). In both cases, the solid state ligand-treated films exhibit only a small degree of surface roughness because the successive layer-by-layer treatment method fills in the cracks formed in previous layers (see Figure S3).

The IR spectra of the PbS CQD films before and after ligand exchange displayed in Figure 1B reveal highly efficient removal of the original oleate ligands in all cases. Solvent was allowed to evaporate from the dry films in an antechamber of a glovebox for 24 h prior to the measurements which were conducted in transmission geometry. For EDT-treated films, the removal of oleate is most clearly observed by the loss of the carboxylate symmetric and asymmetric stretching vibrational absorption bands at ∼1400 and ∼1550 cm^{-1}. The amplitude of the C−H stretch peak in the MPA-treated film spectrum is similar to that of the C−H stretch peak in the EDT-treated film spectrum. EDT and MPA have the same number of C−H bonds per molecule, and the EDT and MPA films have approximately the same thickness in this study. Thus, the similarity of their C−H stretch peak amplitudes indicates comparably complete removal of OA. MPA also has a carboxylate group and therefore exhibits the corresponding absorption bands. It is interesting to note that the strong absorption bands at ∼1400 and ∼1550 cm^{-1} in the vibrational spectrum of the MPA-treated film indicate that essentially all of the carboxylates are—like the thiol groups—bonded to quantum dot surfaces.[30] Free carboxylate groups not bonded to PbS surfaces would appear in the IR spectra around 1700 cm^{-1} (Figure S4). The IR spectra of MPA-treated films demonstrate the absence of free MPA ligands in the ligand-exchanged films. The relatively small frequency difference between the symmetric and asymmetric vibrational modes is consistent with both oxygen atoms of the carboxylate groups being bonded to metal atoms in either chelating or bridging geometries.[30] The absorption features in the spectra at 2350 cm^{-1} arise from small variations in the carbon dioxide content in the infrared spectrometer during the experiments.

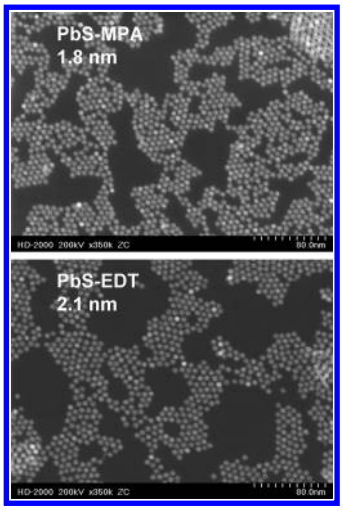

Figure 2. STEM images of 5.0 ± 0.3 nm PbS CQDs passivated by EDT and MPA ligands. Image analysis of the micrographs reveals that the center-to-center spacing of quantum dots depends on the passivating ligand: PbS-MPA films −6.8 ± 0.5 nm and PbS-EDT films −7.1 ± 0.6 nm. From this analysis, average interparticle separations of 1.8 and 2.1 nm are obtained for MPA- and EDT-passivated PbS CQD films, respectively.

The removal of oleate from the nanocrystal surfaces permits the interparticle spacing to decrease, facilitating enhanced electronic coupling between the nanocrystals.[19] The scanning transmission electron microscopy (STEM) images displayed in Figure 2 reveal that the decrease of the average spacing between nanocrystals depends sensitively on the nature of the ligand used to replace OA. The images represent 5.0 ± 0.3 nm PbS nanocrystals that have been treated by 1.15 molar MPA in methanol (top)[5] and 0.119 molar EDT in acetonitrile (bottom).[10] Using image analysis, the average center-to-center spacings of the nanocrystals are determined to be 6.8 ± 0.5 and 7.1 ± 0.6 nm for top and bottom panels, respectively. From these measurements, we estimate the interparticle separation of MPA-treated quantum dots to be 1.8 nm, smaller in comparison to interparticle spacing of 2.1 nm for EDT-capped dots. We note that we used larger 5.0 nm quantum dots for the STEM image analysis because the larger dots are easily observed in the STEM images. Furthermore, the average distance between CQDs in single layers on STEM grids may differ from the average distance between dots in CQD films because the packing of CQDs on STEM grids is less constrained than in solid films. Consequently, the average distances obtained from the STEM images are larger in comparison to

recent measurements of interparticle distances by Nozik and co-workers.[31] Nevertheless, we observe a trend of 10−15% closer packing using MPA compared to EDT when the same metrology is employed.

The mobilities of electrons in the PbS CQD films treated with EDT and MPA were characterized using the ion-gel field-effect transistor geometry. We restrict ourselves to mobility measurements of these two ligands in this discussion because we wish to maintain direct relevance to CQD photovoltaics that we reported recently.[5,10] Using 50 nm layers of the PbS films and a gate electrode consisting of a $LiClO_4$/polyethylene oxide gel contacted by an evaporated gold electrode, n-type current (electron conduction) between the source and drain electrodes, I_d, was measured at a drain voltage of $V_d = 1$ V. Use of the ion-gel technique to measure the minority carrier (electron) mobility in the p-type PbS CQD films is described in detail in Supporting Information. Drain current, I_d, *versus* gate voltage, V_g, for MPA- and EDT-treated PbS CQD films are represented in Figure 3. The inset displays the drain current of EDT-treated films on a logarithmic scale. The drain current of MPA-treated films is more than an order of magnitude larger than that measured in EDT-treated films. The drain current was typically 1000-fold larger in comparison to the gate current, I_g. The field-effect mobility, μ, of the EDT- and MPA-treated films was calculated using the method established by the Frisbie group according to

$$\mu = \frac{LI_d}{WeV_d n}$$
$$n = \int_{V_1}^{V_2} CV_g/AdV_g \qquad (2)$$

where L, W, n, A, V_1, and V_2 are the gate length and width, the accumulated carrier density in the channel, the area of the gate electrode, and the initial and final gate voltages about which I_d-V_g and capacitance *versus* voltage curves are measured, respectively. These measurements in conjunction with eq 2 were used to calculate the electron mobilities in MPA- and EDT-treated CQD films as indicated in Table 1.

Also displayed in Table 1 are the band-tail density of states below the conduction band in MPA- and EDT-treated PbS CQD films. These metrics were reported previously[5,10] being obtained from measurements of the electron acceptor state density (band-tail density) by zero-bias capacitance, depletion width, and built-in voltage of the films. Here, we utilize these previously reported values because we are examining films prepared using identical procedures as those used in the earlier reports. Below, we show that the MPA- and EDT-treated films examined here exhibit similar photovoltaic performance in comparison to materials reported earlier, demonstrating that the mobility and band-tail

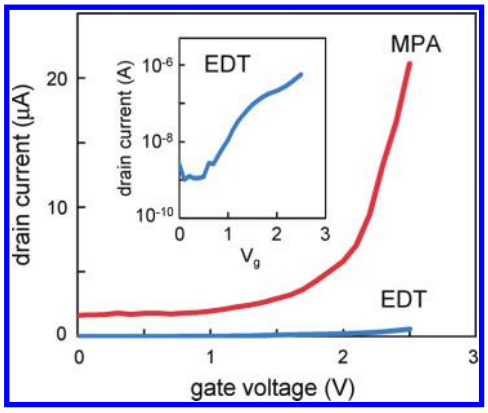

Figure 3. Drain current, I_d, *versus* gate voltage, V_g, measured for minority carriers (electrons) in MPA- and EDT-treated 3.7 nm PbS CQD films measured using the ion-gel field-effect transistor geometry. The inset shows the I_d *versus* V_g curve for EDT-treated films on a logarithmic scale for clarity. The greater drain current of the MPA-treated film is a result of the higher mobility in the CQD film.

TABLE 1. Electrical Properties of PbS CQD Films Treated with EDT and MPA Ligands

	PbS-EDT	PbS-MPA
$\mu\langle\tau\rangle$ product (arb. unit)	0.022	0.16
μ ($cm^2/V\cdot s$)	2.4×10^{-4}	5.1×10^{-3}
$\langle\tau\rangle$ (μs)	93	31
$\langle E\rangle$ (eV)	0.29	0.27
band-tail density of states		
TRIR (arb. unit)	3.3	1.0
$C-V_g$ (cm^{-3})	8×10^{16}	2×10^{16}

density of states established in those earlier reports[5,10] are applicable to the present materials.

Time-resolved infrared spectroscopy was used to examine PbS CQD films treated with various ligand strategies. The experimental geometry of the TRIR measurements is represented in Figure 4A. A 10 ns duration 532 nm optical pump pulse is used to excite the band gap of the PbS CQD films, resulting in fast generation of electrons and holes that are examined by a continuum infrared probe. The transient IR spectra displayed in Figure 4B were measured in MPA- and EDT-treated PbS CQD films 500 ns following the excitation laser pulse. The transient spectra have been scaled to account for small differences in absorbance at the pump excitation wavelength such that the amplitudes of the spectra can be quantitatively compared. As the time delay following the excitation pulse increases, the amplitudes of the spectra decrease while their shapes remain constant in all cases.

Two characteristic features are observed in the transient spectra: narrow vibrational features of ligands attached to the PbS CQD surfaces and broad electronic transitions. As we show in the Discussion section, the electronic transitions provide information about charge trapping and charge recombination in the ligand-treated CQD films. The PbS CQD films used in the TRIR

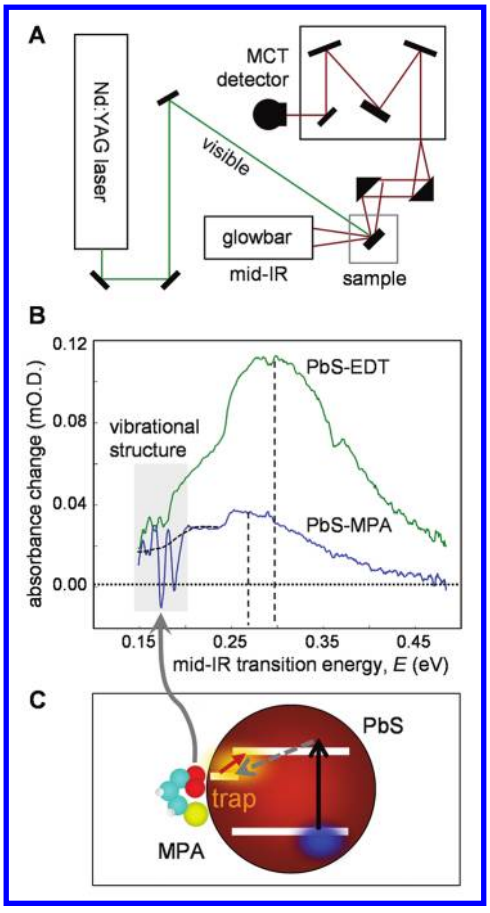

Figure 4. (A) Schematic diagram of the TRIR spectrometer configuration used to measure infrared transient absorption spectra of 3.7 nm PbS CQD films. (B) TRIR spectra of PbS CQD films passivated by EDT and MPA ligands. The narrow spectral features appearing at 0.15–0.2 eV (1200–1600 cm^{-1}) arise from transient vibrational features of ligands that are perturbed by the formation of charge traps at the ligand–nanocrystal interfaces. The broad absorption features correspond to electronic transitions where trapped electrons (holes) are excited back into delocalized states of the quantum dots. The average frequencies of the PbS CQD films, indicated by the dashed lines, depend sensitively on the ligand used to passivate the PbS quantum dot surfaces. (C) Schematic diagram illustrating how ligand vibrational modes are perturbed by changes in charge distribution at quantum dot surfaces when electrons become trapped.

measurements were fabricated using the same procedures and number of layer-by-layer cycles as those used to fabricate test structures for the electrical measurements (see Methods section).

DISCUSSION

Assignment of Trap-to-Band Transitions. We turn now to consider the correlation of the electrical and optical measurements that enable us to obtain mobility-lifetime products of the CQD films. We first consider the assignment of transient absorption features appearing in the TRIR spectra displayed in Figure 4B. Two distinct types of transient absorption features are apparent in the spectra: first, characteristically narrow vibrational features of the ligands appear between 0.15 and 0.2 eV (1200–1600 cm^{-1}); and second, broad absorptions arising from electronic transitions. On ultrafast (picosecond) time scales, band gap excitation of CQDs has been shown to give rise to broad intraband transitions in the mid-IR in which electrons (holes) in their lowest energy delocalized $1S_{e(h)}$ states transition to higher energy $1P_{e(h)}$ states within the electronic state manifold.[32–38] The average frequencies at which such intraband transitions occur have been shown to be strongly correlated with the band gap or interband transitions of quantum dots.[36] Broad, long-lived absorptions in the mid-IR have also been observed on the microsecond time scale similar to those represented in Figure 4B.[33] These absorptions were initially assigned to intraband transitions but later were reinterpreted in terms of absorptions due to trapped carriers.[35,38] The rationale was that, on longer time scales, delocalized electrons (holes) may become localized in charge trap or surface states as they are given time to fully sample their energetic landscape. Trap-to-band transitions can be distinguished from intraband transitions on the basis of their relative sensitivity to the surface chemistry of the CQDs. For example, Guyot-Sionnest showed that spectra of intraband transitions are not strongly sensitive to the chemical treatment of CdSe CQDs in solution,[33] although surface ligands do strongly influence the intraband relaxation dynamics.[35] These trapped electrons (holes) can be excited back into delocalized states by absorbing photons of energy greater than or equal to their trapping energy.[38]

To establish the origin of the broad absorption features appearing in Figure 4B that are observed on longer time scales (500 ns), we investigated correlations between the average frequency of the mid-IR absorptions and the corresponding band gap absorptions of a series of PbS CQD films treated with various ligands. We measured the $1S_h$–$1S_e$ band gap transitions of CQD films treated with the ligand series: MPA, EDT, 1,3-propane dithiol (PrDT), 1,4-butane dithiol (BDT), 1,5-pentane dithiol (PnDT), 1,6-hexane dithiol (HDT), orthobenzene dithiol (1,2-BzDT), and parabenzene dithiol (1,4-BzDT). We based the ligand exchange procedures for the dithiols on those used to fabricate EDT-treated CQD films.[5] The IR absorption spectra of the films demonstrating complete removal of the original oleic acid ligands are represented in Figure S4.

We measured near-IR absorption spectra of the ligand-exchanged PbS CQD films to characterize their band gap ($1S_h$–$1S_e$) transitions. Although the same batch of oleic-acid-capped PbS CQDs were used as the starting materials for each film, the near-IR spectra represented in Figure S5 demonstrate about 0.07 eV variation in the band gaps of the CQD films. The observed range of band gaps arises from variations of the interdot coupling[39] in the films, variations of ligand–nanocrystal interactions, and possibly the influence of ligands on the dielectric properties of the films.[40,41] For

example, EDT-treated CQD films exhibit lower energy band gap transitions than do HDT-treated films, consistent with a larger average interparticle separation obtained from the HDT treatment. The bulkier HDT ligands reduce the electronic coupling between neighboring quantum dots, giving rise to a greater degree of quantum confinement and a higher energy band gap transition in comparison to EDT-treated films.

We measured spectra of the broad electronic transitions in the mid-IR arising from band gap excitation of the corresponding PbS CQD films treated with the set of ligands using TRIR spectroscopy. The TRIR spectra represented in Figure S6 display significant variation in shape and intensity of the electronic transitions measured in the set of ligand-exchanged films. In particular, we observe approximately 0.13 eV variation of the peak of the mid-IR transition energies among the ligand-treated films. It is notable that the device relevant ligand treatment strategies (MPA and EDT) exhibit the lowest TRIR signal amplitudes and the lowest mid-IR transition energies.

We correlated the band gap transitions of the ligand-treated CQD films with the corresponding mid-IR electronic transition energies measured with TRIR spectroscopy. We reasoned that if the electronic transitions observed in the TRIR spectra arise from intraband transitions, similar to recent reports by Guyot-Sionnest,[36] then we should observe clear correlations between the band gap and mid-IR transition energies. Figure 5 correlates the center of the $1S_h-1S_e$ band gap transitions obtained from near-IR spectra of the PbS CQD films (displayed in Figure S5) with the corresponding average transition energies measured from the TRIR spectra. The average transition energies are calculated from the TRIR spectra in Figure S6 according to

$$\langle E \rangle = \int Eg(E)\mathrm{d}E / \int g(E)\mathrm{d}E \qquad (3)$$

where $g(E)$ represents the broad absorption line shape in the TRIR spectra expressed in terms of the transition energy, E. We chose to compare the spectra using their weighted average transition energies because the approach does not require us to adopt a particular line shape in order to quantify the center frequencies of the mid-IR electronic transitions.

The data in Figure 5 indicate that some correlation may exist between the band gap and the mid-IR transition energies of the ligand-exchanged films, but any correlation present is overwhelmed by scatter due to variation of ligand–nanocrystal interactions associated with changes in ligand molecular structure. The dotted line in the figure reflects the expected correlation with the $1S_h-1S_e$ transition energies if the broad absorption in the TRIR spectra arose from intraband transitions.[36] The dominant influence of ligand molecular structure on the mid-IR electronic absorption features indicates that the absorption arises from states that are more strongly influenced by the chemical

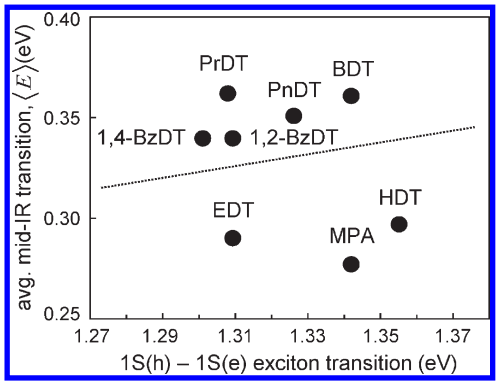

Figure 5. Comparison of the band gap transition energies with the corresponding average mid-IR transition energies of 3.7 nm PbS CQD films treated with various ligands: MPA, EDT, 1,3-propane dithiol (PrDT), 1,4-butane dithiol (BDT), 1,5-pentane dithiol (PnDT), 1,6-hexane dithiol (HDT), ortho-benzene dithiol (1,2-BzDT), and parabenzene dithiol (1,4-BzDT). The average mid-IR transition energies are obtained according to eq 3. The data exhibit a trend with variation of the band gap, but the trend is overwhelmed by scatter due to variation in ligand–nanocrystal interactions with changes in molecular structure.

identity of the ligands than by the band gap of the quantum dots. Although TRIR spectroscopy is not surface-specific and so cannot directly distinguish surface from bulk states, we believe that the states involved in the broad electronic transitions primarily reside at CQD surfaces because purely surface modifications have such a strong influence on the spectra of the transitions. On the basis of these observations, we assign the broad electronic transitions in the TRIR spectra to transitions of electrons (holes) from localized states (band-tail or trap states) to delocalized core states of the CQDs.

The observation of ligand vibrational features superimposed on the broad electronic transitions in the TRIR spectra (Figure 4B) provides further evidence in support of the trap to delocalized state transition assignment. The schematic in Figure 4C depicts pictorially the photophysical sequence that gives rise to the vibrational features for the case of electrons. Photoexcitation of the band gap of the CQDs creates excitons (vertical arrow). On the submicrosecond time scale, electrons (holes) become trapped, changing the charge distribution experienced by ligands near the localized trap states (dashed arrow). The mid-IR probe beam probes the transitions of the localized electrons (holes) back into delocalized core states (small diagonal arrow).[38]

The corresponding changes in charge distribution at quantum dot surfaces due to charge trapping give rise to two sets of vibrational features in the TRIR spectra. The vibrational features are most pronounced in the case of MPA-treated films because carboxylate groups are strong infrared chromophores and they are directly connected to the quantum dot surfaces. Sharp negative-going features around 0.18 eV (1405 and 1520 cm^{-1}) indicate the vibrational spectra of the

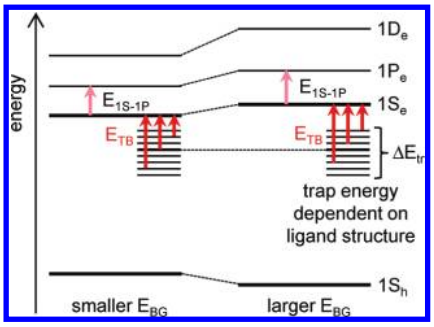

Figure 6. Schematic diagram illustrating the dependence of intraband *versus* trap-to-band transitions on quantum dot band gap and surface chemistry. The spectra of intraband transitions vary with the band gap but are relatively insensitive to variation of ligand–nanocrystal interactions. In contrast, trap-to-band transitions are sensitive to both the band gap and ligand–nanocrystal interactions. The large ligand-related scatter in Figure 5 coupled with the perturbation of ligand vibrational modes (Figure 4B) indicates that the mid-IR absorption results from trap-to-band transitions rather than intraband transitions.

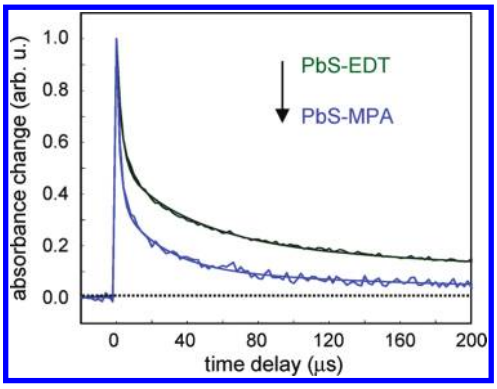

Figure 7. Transient absorption kinetics traces of 3.7 nm PbS CQD films passivated with MPA and EDT ligands. The kinetics traces were measured at the peaks of the trap-to-band electronic transitions measured in the TRIR spectra and have been normalized to facilitate comparison of their decay dynamics. Analysis of the kinetics traces according to eq 4 reveals that MPA-passivated PbS CQD films undergo charge recombination 3-fold faster in comparison to EDT-passivated films (see Table 1).

carboxylate group of MPA before electrons (holes) are localized in the vicinity of the ligands. These features have a negative sign because photoexcitation of the CQDs reduces the concentration of the unperturbed MPA ligands that are found in the ground state of the system. Near these vibrational features in the spectra are small positive-going peaks indicating the spectra of ligands that are in the vicinity of localized charges. They are new absorptions resulting from photoexcitation and so have a positive sign in the spectra. It is useful to point out that, if the broad electronic transitions in the TRIR spectra arose from intraband transitions, it is unlikely that vibrational features would be observed because there would not be large changes in charge distribution at the quantum dot surfaces. Indeed, no discernible vibrational features are observed in the spectra of intraband transitions of CdSe CQDs in solution reported by Guyot-Sionnest.[33]

It is the combination of the dominant influence of ligands on the mid-IR transition energies (Figure 5) with the appearance of vibrational features in the TRIR spectra (Figure 4B) that lead us to assign the broad electronic transitions as trap to delocalized state transitions rather than intraband transitions. We will henceforth refer to the mid-IR electronic transitions observed in the TRIR spectra as trap-to-band transitions.

The energy diagram appearing in Figure 6 summarizes the observations and interpretation detailed above. Energy diagrams of two CQDs of differing band gaps are depicted focusing on electrons. Equivalent diagrams exist for holes. Intraband transitions such as those reported by Guyot-Sionnest are represented as $E_{1S\text{-}1P}$ in the diagram.[33] The energy of these transitions increases with larger band gaps as has been reported.[33,36] Trap-to-band transitions are also depicted in the diagram as E_{TB} that involve promotion of electrons (holes) from localized trap states to delocalized core states.[38] Weak mixing of localized states with delocalized core states causes the localized state energies to change little with variation in the quantum confined band gap. Therefore, trap-to-band transitions exhibit some correlation with the band gaps of quantum dots because the energy of the final state in the transition does depend on the band gap.[38] However, ligand–nanocrystal interactions strongly influence the energies of localized states residing primarily at surfaces such that a range of ligand structures results in a significant span of surface state energies, represented as ΔE_{tr} in Figure 6. Therefore, trap-to-band transitions are more strongly influenced by the chemical identity of the ligands than by the band gap of the quantum dots, unlike intraband transitions.[33]

We point out that the underlying origin of surface state energy variation with ligand molecular structure is a topic of ongoing investigation. One possibility is that ligand–nanocrystal interactions that depend sensitively on ligand structure influence the polarization of electronic wave functions of the CQD cores[42] giving rise to variations in trap-to-band transition energies. This subject will be the topic of a forthcoming publication. The average transition energies, $\langle E \rangle$, obtained from TRIR spectra displayed in Figure 4B for EDT- and MPA-treated PbS CQD films are tabulated in Table 1.

Variation in Mobility-Lifetime Products. Having established that the broad absorption features in the TRIR spectra in Figure 4B and Figure S6 arise from trap-to-band transitions, we interpret the time-dependent decay of these signals as a direct measure of the charge recombination kinetics. We plot in Figure 7 the time-dependent amplitudes of trap-to-band transitions in MPA- and EDT-treated CQD films that were measured at the maxima of the absorption features. Because the transient spectra undergo negligible change in shape within our time resolution (~300 ns), an amplitude

measurement is sufficient to characterize the transient population dynamics. The kinetics traces have been normalized to facilitate comparison of their relative decay profiles.

To quantify the charge recombination kinetics, we calculated the average lifetime from kinetics displayed in Figure 7 according to

$$\langle\tau\rangle = \int_0^\infty tf(t)dt / \int_0^\infty f(t)dt \qquad (4)$$

where $f(t)$ represents the experimental kinetics decay trace for a given sample. Average lifetimes, $\langle\tau\rangle$, of 93 and 31 μs for EDT and MPA are obtained from eq 4 and tabulated in Table 1. It is interesting to note that the electron mobility comparing EDT- and MPA-treated films increases more than a factor of 20, while the recombination lifetime decreases by only a factor of 3.

We note that charge recombination has been observed on the submicrosecond time scale in fully depleted PbS CQD photodetectors treated with benzene dithiol using time-dependent short-circuit current measurements.[43] The difference in time scales obtained from the TRIR and transient short-circuit current measurements is likely a result of the dissimilar sensitivity of the measurement techniques to charge trapping. For example, it is challenging to distinguish charge trapping from charge recombination in time-dependent short-circuit current measurements because both processes lead to a loss of photocurrent. In contrast, mobile carriers (which likely undergo intraband transitions) and trapped carriers still contribute to the signal in TRIR experiments. Indeed, if charge trapping does occur on the submicrosecond time scale, we would observe the tail end of this process as a fast spike convolved with the ~300 ns response function of the TRIR instrument. The analysis scheme we employ minimizes potential interference from intraband transitions by calculating a time constant *via* integration of the entire kinetic decay. Using this approach, we find that charge recombination occurs more quickly in the higher mobility MPA-treated CQD films as expected from a diffusion controlled process.[44]

Comparison of mobility and lifetime data in Table 1 reveals that the mobility-lifetime products of charge carriers increased by a factor of more than seven comparing EDT- and MPA-treated PbS CQD films. The increase in the mobility-lifetime products is counter to predictions from mean field theories of diffusion-controlled bimolecular charge recombination that predict an inverse proportionality between the charge recombination lifetime and the carrier mobility.[44] Such proportionality of mobility and lifetime has been observed in certain organic photovoltaic materials, for example.[45−47]

We suggest that the charge recombination lifetimes do not decrease as steeply as the mobilities increase because of changes in the density of charge traps in the PbS CQD films. Previous measurements of the band-tail density of states below the conduction band in MPA[10]- and EDT[5]-treated PbS CQD films reveal that MPA-treated films possess approximately one-fourth as many charge traps below the conduction band edge in comparison to EDT-treated films (Table 1). The variation in band-tail density of states is in good agreement with the integrated areas of the transient spectra represented in Figure 4B that arise from the absorption of trapped charges (that are trapped in band-tail states). The ratio of electrically measured band-tail densities is N_{EDT}:N_{MPA} = 4:1, and the ratio of integrated areas of the TRIR spectra is A_{EDT}:A_{MPA} = 3.3:1. We therefore conclude that the band-tail density of states is proportional to the density of trapped charges as determined by TRIR spectroscopy. Thus, although EDT-treated PbS CQD films have lower electron mobility, the average separation between trapped charges is smaller, resulting in proportionately faster recombination. The lower trap density in MPA-treated PbS CQD films results in, on average, larger separation between trapped carriers giving rise to proportionately slower charge recombination. In total, these observations lead us to conclude that it is the combination of three factors, smaller interparticle spacing, lower charge trap depth, and lower charge trap density, that favorably influences both the carrier mobility and recombination lifetime resulting in the 7-fold increase in the mobility-lifetime product comparing EDT- and MPA-treated films.

Influence of Mobility-Lifetime Products on Devices. The fundamental study described above suggests that MPA-treated CQD films should exhibit markedly better transport in comparison to EDT-treated films due to lower band-tail density of states and energetic distribution near the conduction band. We sought to investigate whether these improvements translate into the expected enhancement in photovoltaic performance. We built devices consisting of a Zr-doped TiO_2 electrode on which the quantum dot films were deposited. The devices were capped using a Au contact. In these devices, a depleted heterojunction is formed at the {n-type-TiO_2}-to-{p-type-quantum-dot-film} interface, resulting in electron extraction into the titania and hole extraction *via* the gold ohmic contact.

To quantitatively compare the impact of improved transport on device performance, we kept all aspects of the devices identical including matching the thickness of the quantum dot layers so that they have the same optical densities for equal light absorption. The only property of the devices we varied was the treatment of the quantum dot film between MPA and EDT. Figure 8A,B depict current−voltage curves measured in MPA- and EDT-treated devices under simulated AM1.5 solar illumination, respectively. The detailed conditions under which the photovoltaic performance was measured are described in Supporting Information. The most striking improvement in the case of MPA is in the

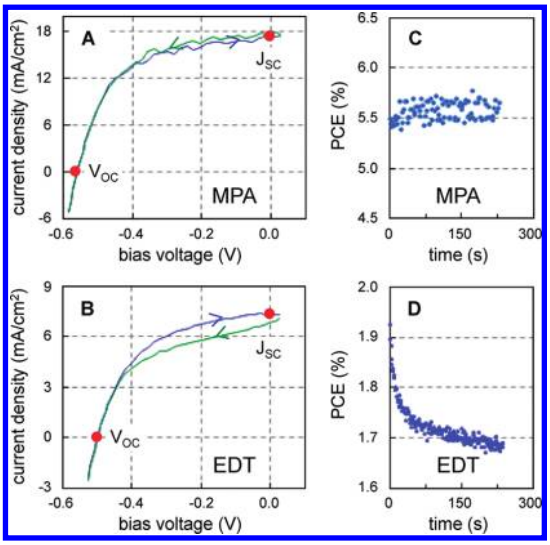

Figure 8. Current–voltage characteristics of MPA-treated (A) and EDT-treated (B) PbS CQD devices with the bias voltage swept in both the increasing and decreasing directions (see arrows). The MPA-treated device produces short-circuit current, J_{SC}, that is twice as large as that produced by the EDT-treated device, consistent with improved transport in the MPA-treated device. The open-circuit voltage, V_{OC}, of the MPA-treated device is slightly greater than the V_{OC} of the EDT-treated device. Plot of the temporal stability of maximum power conversion efficiency (PCE) point for MPA-treated (C) and EDT-treated (D) devices. Interestingly, the MPA-treated device is more stable in comparison to the EDT-treated device.

short-circuit current density, J_{SC}, which is twice as large as the J_{SC} measured in the EDT-treated device, consistent with improved transport due to higher minority carrier (electron) mobility and superior reduction of band-tail states as reported above and in Table 1. The overall performance of the MPA-treated device (see Figure 8C,D) was substantially better due to the higher J_{SC} and slightly greater open-circuit voltage. Interestingly, the stability of the MPA-treated device power conversion efficiency in time is superior in comparison to the EDT-treated device.

CONCLUSIONS AND IMPLICATIONS

Through a combination of electrical and optical measurements, we have demonstrated that the choice of ligand passivation strategy strongly influences the charge carrier mobility and recombination properties of PbS CQD films. In particular, a new passivation strategy based on 3-mercaptopropionic acid (MPA) enables significant enhancement of the mobility-lifetime products of PbS CQD films leading to increases in both the diffusion lengths of charge carriers and the power conversion efficiencies of PbS CQD photovoltaic test structures. The origin of the enhanced mobility-lifetime products enabled by the MPA passivation strategy is traced to a lower density and energetic distribution of charge traps in MPA-treated PbS CQD films as determined from time-resolved infrared spectroscopy and capacitance measurements. The shallower trap state energy distribution enables higher carrier mobility for faster charge transport. Simultaneously, the lower density of charge traps decreases the bimolecular charge recombination rate in comparison to the rate expected from the increase in carrier mobility. Direct comparison of devices with identical architectures and differing only by the ligand treatment strategy reveals that improvements of the mobility-lifetime products do in fact translate into superior photovoltaic performance.

An important implication of the present findings is that judicious selection of novel ligand passivants and processing conditions is a promising route to greater charge carrier diffusion lengths in CQD films. For example, MPA provides greater chemical diversity in comparison to EDT (presenting both thiol and carboxylate functional groups to PbS surfaces) and is therefore able to passivate a broader distribution of surface states. Our findings suggest that the ideal ligand passivant should be capable of passivating a diversity of surface states that are found in CQDs while maintaining close contact between neighboring dots for fast electrical transport. This combined electrical and optical investigation demonstrates conclusively that development of novel ligand passivation strategies providing longer diffusion lengths will enable more efficient utilization of the near-IR region of the solar spectrum in PbS CQD photovoltaic devices.

METHODS

PbS CQDs were synthesized according to published procedures.[48] TiO_2 substrates were fabricated from zirconium-doped titania synthesized using a sol–gel technique. The titania sol–gel was spin-cast onto fluorine-doped tin-oxide-coated substrates and sintered to remove the organic phase. PbS CQD films were deposited onto the titania substrates using layer-by-layer assembly. Films passivated by EDT and MPA were prepared under ambient conditions according to literature procedures.[5,10] Identical steps were used to deposit PbS CQD films for both the electrical and TRIR characterization experiments. For the electrical measurements, contacts consisting of 20 nm of Au followed by 100 nm of Ag were deposited with an active area of 6.07 mm^2.

Current–voltage measurements were conducted with Keithley 2400 source meters in N_2 environment using the ion-gel field-effect transistor configuration developed by Frisbie.[49,50] One source meter acquired the drain–source current, while a second source meter measured the gate–source current. Capacitance–voltage measurements were performed on field-effect transistor test structures in nitrogen atmosphere using an Agilent LCR meter set to 20 Hz ac signal.

TRIR spectroscopy experiments were performed on a home-built instrument that has been described elsewhere.[51] Briefly, a nanosecond duration 532 nm excitation pulse was used to excite the band gap of PbS CQD films. The films were deposited onto an aluminum-coated mirror, and a reflective optical geometry was utilized for the TRIR experiments, as has been

described previously.[52,53] The excitation energy density of 500 μJ/cm^2 was selected such that approximately one photon impinged on the sample per quantum dot in the film. The same excitation density was used for both EDT- and MPA-treated films, and both films exhibited similar optical absorptions at 532 nm. TRIR spectra were measured using a continuous wave infrared glowbar light source. The infrared continuum was dispersed in a monochromator, and transient absorption kinetics traces were measured at each wavelength using a mercury cadmium telluride (MCT) detector tied to a fast digitizer. PbS CQD films examined in the TRIR experiments were prepared under identical conditions as were the films prepared for the electrical measurements.

Acknowledgment. This research was supported in part by the Petroleum Research Fund under Grant No. PRF #49639-ND6, the National Science Foundation under Grant No. 0846241, and the Office of Naval Research under Grant No. N00014-11-1-0239. This publication is also based in part on work supported by Award No. KUS-11-009-21, made by King Abdullah University of Science and Technology (KAUST).

Supporting Information Available: Detailed list of chemicals used, methods of synthesis and purification of PbS CQDs, methods for preparing PbS CQD films, methods for photovoltaic device characterization, methods for field-effect mobility measurements, analysis of CQD size distribution, microscopy of ligand-exchanged CQD films, and characterization of ligand-exchanged CQD films using IR, near-IR, and TRIR spectroscopy. This material is available free of charge *via* the Internet at http://pubs.acs.org.

REFERENCES AND NOTES

1. Green, M. A.; Emery, K.; Hishikawa, Y.; Warta, W. Solar Cell Efficiency Tables (Version 35). *Prog. Photovoltaics* **2010**, *18*, 144–150.
2. Tang, J.; Sargent, E. H. Infrared Colloidal Quantum Dots for Photovoltaics: Fundamentals and Recent Progress. *Adv. Mater.* **2011**, *23*, 12–29.
3. Wang, X.; Koleilat, G. I.; Tang, J.; Liu, H.; Kramer, I. J.; Debnath, R.; Brzozowski, L.; Barkhouse, A. R.; Levina, L.; Hoogland, S.; Sargent, E. H. Tendem Colloidal Quantum Dot Solar Cells Employing a Graded Recombination Layer. *Nat. Photonics* **2011**, *5*, 480–484.
4. Johnston, K. W.; Pattantyus-Abraham, A. G.; Clifford, J. P.; Myrskog, S. H.; MacNeil, D. D.; Levina, L.; Sargent, E. H. Schottky-Quantum Dot Photovoltaics for Efficient Infrared Power Conversion. *Appl. Phys. Lett.* **2008**, *92*, 151115(3).
5. Tang, J.; Brzozowski, L.; Barkhouse, D. A. R.; Wang, X.; Debnath, R.; Wolowiec, R.; Palmiano, E.; Levina, L.; Pattantyus-Abraham, A. G.; Jamakosmanovic, D.; Sargent, E. H. Quantum Dot Photovoltaics in the Extreme Quantum Confinement Regime: The Surface-Chemical Origins of Exceptional Air- and Light-Stability. *ACS Nano* **2010**, *4*, 869–878.
6. Debnath, R.; Tang, J.; Barkhouse, D. A. R.; Wang, X.; Pattantyus-Abraham, A. G.; Brzozowski, L.; Levina, L.; Sargent, E. H. Ambient-Processed Colloidal Quantum Dot Solar Cells *via* Individual Pre-encapsulation of Nanoparticles. *J. Am. Chem. Soc.* **2010**, *132*, 5952–5953.
7. Zhao, N.; Osedach, T. P.; Chang, L. Y.; Geyer, S. M.; Wanger, D.; Binda, M. T.; Arango, A. C.; Bawendi, M. G.; Bulovic, V. Colloidal PbS Quantum Dot Solar Cells with High Fill Factor. *ACS Nano* **2010**, *4*, 3743–3752.
8. Luther, J. M.; Law, M.; Beard, M. C.; Song, Q.; Reese, M. O.; Ellingson, R. J.; Nozik, A. J. Schottky Solar Cells Based on Colloidal Nanocrystal Films. *Nano Lett.* **2008**, *8*, 3488–3492.
9. Ma, W.; Luther, J. M.; Zheng, H.; Wu, Y.; Alivisatos, A. P. Photovoltaic Devices Employing Ternary PbS_xSe_{x-1} Nanocrystals. *Nano Lett.* **2009**, *9*, 1699–1703.
10. Pattantyus-Abraham, A. G.; Kramer, I. J.; Barkhouse, A. R.; Wang, X.; Konstantatos, G.; Debnath, R.; Levina, L.; Nazeeruddin, M. K.; Gratzel, M.; Sargent, E. H. Depleted-Heterojunction Colloidal Quantum Dot Solar Cells. *ACS Nano* **2010**, *4*, 3374–3380.
11. Luther, J. M.; Gao, J.; Lloyd, M. T.; Semonin, O. E.; Beard, M. C.; Nozik, A. J. Stability Assessment on a 3% Bilayer PbS/ZnO Quantum Dot Heterojunction Solar Cell. *Adv. Mater.* **2010**, *22*, 3704–3707.
12. Choi, J. J.; Lim, Y.-F.; Santiago-Berrios, M. B.; Oh, M.; Hyun, B.-R.; Sun, L.; Bartnik, A. C.; Goedhard, A.; Malliaras, G. G.; Abruna, H. D.; Wise, F. W.; Hanrath, T. PbSe Nanocrystal Excitonic Solar Cells. *Nano Lett.* **2009**, *9*, 3749–3755.
13. Leschkies, K. S.; Beatty, T. J.; Kang, M. S.; Norris, D. J.; Aydil, E. S. Solar Cells Based on Junctions Between Colloidal PbSe Nanocrystals and Thin ZnO Films. *ACS Nano* **2009**, *3*, 3638–3648.
14. Leschkies, K. S.; Jacobs, A. G.; Norris, D. J.; Aydil, E. S. Nanowire-Quantum-Dot Solar Cells and the Influence of Nanowire Length on the Charge Collection Efficiency. *Appl. Phys. Lett.* **2009**, *95*, 193103(3).
15. Tsang, S. W.; Fu, H.; Wang, R.; Lu, J.; Yu, K.; Tao, Y. Highly Efficient Cross-Linked PbS Nanocrystal/C60 Hybrid Heterojunction Photovoltaic Cells. *Appl. Phys. Lett.* **2009**, *95*, 183505(3).
16. Johnston, K. W.; Pattantyus-Abraham, A. G.; Clifford, J. P.; Myrskog, S. H.; Hoogland, S.; Shukla, H.; Klem, E. J. D.; Levina, L.; Sargent, E. H. Efficient Schottky-Quantum-Dot Photovoltaics: The Roles of Depletion, Drift, and Diffusion. *Appl. Phys. Lett.* **2008**, *92*, 122111(3).
17. Koleilat, G. I.; Levina, L.; Shukla, H.; Myrskog, S. H.; Hinds, S.; Pattantyus-Abraham, A. G.; Sargent, E. H. Efficient, Stable Infrared Photovoltaics Based on Solution-Cast Colloidal Quantum Dots. *ACS Nano* **2008**, *2*, 833–840.
18. Barkhouse, D. A. R.; Debnath, R.; Kramer, I. J.; Zhitomirsky, D.; Pattantyus-Abraham, A. G.; Levina, L.; Etgar, L.; Gratzel, M.; Sargent, E. H. Depleted Bulk Heterojunction Colloidal Quantum Dot Photovoltaics. *Adv. Mater.* **2011**, *23*, 3134–3138.
19. Talapin, D. V.; Lee, J.-S.; Kovalenko, M. V.; Shevchenko, E. V. Prospects of Colloidal Nanocrystals for Electronic and Optoelectronic Applications. *Chem. Rev.* **2010**, *110*, 389–458.
20. Sargent, E. H. Infrared Photovoltaics Made by Solution Processing. *Nat. Photonics* **2009**, *3*, 325–331.
21. Milliron, D. J.; Gur, I.; Alivisatos, A. P. Hybrid Organic-Nanocrystal Solar Cells. *MRS Bull.* **2005**, *30*, 41–44.
22. Gur, I.; Fromer, N. A.; Chen, C.-P.; Kanaras, A. G.; Alivisatos, A. P. Hybrid Solar Cells with Prescribed Nanoscale Morphologies Based on Hyperbranched Semiconductor Nanocrystals. *Nano Lett.* **2007**, *7*, 409–414.
23. Talapin, D. V.; Murray, C. B. PbSe Nanocrystal Solids for n- and p-Channel Thin Film Field-Effect Transistors. *Science* **2005**, *310*, 86–89.
24. Urban, J. J.; Talapin, D. V.; Shevchenko, E. V.; Murray, C. B. Self-Assembly of PbTe Quantum Dots into Nanocrystal Superlattices and Glassy Films. *J. Am. Chem. Soc.* **2006**, *128*, 3248–3255.
25. Sun, B.; Findikoglu, A. T.; Sykora, M.; Werder, D. J.; Klimov, V. I. Hybrid Photovoltaics Based on Semiconductor Nanocrystals and Amorphous Silicon. *Nano Lett.* **2009**, *9*, 1235–1241.
26. Kovalenko, M. V.; Scheele, M.; Talapin, D. V. Colloidal Nanocrystals with Molecular Metal Chalcogenide Surface Ligands. *Science* **2009**, *324*, 1417–1420.
27. Kovalenko, M. V.; Bodnarchuk, M. I.; Zaumseil, J.; Lee, J.-S.; Talapin, D. V. Expanding the Chemical Versatility of Colloidal Nanocrystals Capped with Molecular Metal Chalcogenide Ligands. *J. Am. Chem. Soc.* **2010**, *132*, 10085–10092.
28. Porter, V. J.; Geyer, S.; Halpert, J. E.; Kastner, M. A.; Bawendi, M. G. Photoconductivity in Annealed and Chemically Treated CdSe/ZnS Inorganic Nanocrystal Films. *J. Phys. Chem. C* **2008**, *112*, 2308–2316.
29. Geyer, S.; Porter, V. J.; Halpert, J. E.; Mentzel, T. S.; Kastner, M. A.; Bawendi, M. G. Charge Transport in Mixed CdSe and CdTe Colloidal Nanocrystal Films. *Phys. Rev. B* **2010**, *82*, 155201(8).
30. Deacon, G. B.; Phillips, R. J. Relationships between the Carbon–Oxygen Stretching Frequencies of Carboxylato Complexes and the Type of Carboxylate Coordination. *Coord. Chem. Rev.* **1980**, *33*, 227–250.
31. Beard, M. C.; Midgett, A. G.; Law, M.; Semonin, O. E.; Ellingson, R. J.; Nozik, A. J. Variations in the Quantum

Efficiency of Multiple Exciton Generation for a Series of Chemically Treated PbSe Nanocrystal Films. *Nano Lett.* **2009**, *9*, 836–845.
32. Guyot-Sionnest, P.; Shim, M.; Matranga, C.; Hines, M. Intraband Relaxation in CdSe Quantum Dots. *Phys. Rev. B* **1999**, *60*, R2181–R2184.
33. Shim, M.; Shilov, S. V.; Braiman, M. S.; Guyot-Sionnest, P. Long-Lived Delocalized Electron States in Quantum Dots: A Step-Scan Fourier Transform Infrared Study. *J. Phys. Chem. B* **2000**, *104*, 1494–1496.
34. Shim, M.; Guyot-Sionnest, P. Intraband Hole Burning in Colloidal Quantum Dots. *Phys. Rev. B* **2001**, *64*, 245342(4).
35. Guyot-Sionnest, P.; Wehrenberg, B.; Yu, D. Intraband Relaxation in CdSe Nanocrystals and the Strong Influence of the Surface Ligands. *J. Chem. Phys.* **2005**, *123*, 074709(7).
36. Pandey, A.; Guyot-Sionnest, P. Intraband Spectroscopy and Band Offsets of Colloidal II–VI Core/Shell Structures. *J. Chem. Phys.* **2007**, *127*, 104710(10).
37. Harbold, J. M.; Du, H.; Krauss, T. D.; Cho, K.-S.; Murray, C. B.; Wise, F. W. Time-Resolved Intraband Relaxation of Strongly Confined Electrons and Holes in Colloidal PbSe Nanocrystals. *Phys. Rev. B* **2005**, *72*, 195312(6).
38. Zhang, J.; Jiang, X. Confinement-Dependent Below-Gap State in PbS Quantum Dot Films Probed by Continuous-Wave Photoinduced Absorption. *J. Phys. Chem. B* **2008**, *112*, 9557–9560.
39. Williams, K. J.; Tisdale, W. A.; Leschkies, K. S.; Haugstad, G.; Norris, D. J.; Aydil, E. S.; Zhu, X.-Y. Strong Electronic Coupling in Two-Dimensional Assemblies of Colloidal PbSe Quantum Dots. *ACS Nano* **2009**, *3*, 1532–1538.
40. Rodina, A. V.; Efros, A. L. Band-Edge Biexciton in Nanocrystals of Semiconductors with a Degenerate Valence Band. *Phys. Rev. B* **2010**, *82*, 125324(14).
41. Bartnik, A. C.; Efros, A. L.; Koh, W.-K.; Murray, C. B.; Wise, F. W. Electronic States and Optical Properties of PbSe Nanorods and Nanowires. *Phys. Rev. B* **2010**, *82*, 195313(16).
42. Wolcott, A.; Doyeux, V.; Nelson, C. A.; Gearba, R.; Lei, K. W.; Yager, K. G.; Dolocan, A. D.; Williams, K.; Nguyen, D.; Zhu, X.-Y. Anomalously Large Polarization Effect Responsible for Excitonic Red Shifts in PbSe Quantum Dot Solids. *J. Phys. Chem. Lett.* **2011**, *2*, 795–800.
43. Clifford, J. P.; Konstantatos, G.; Johnston, K. W.; Hoogland, S.; Levina, L.; Sargent, E. H. Fast, Sensitive and Spectrally Tuneable Colloidal Quantym-Dot Photodetectors. *Nat. Nanotechnol.* **2009**, *4*, 40–44.
44. Waite, T. R. Theoretical Treatment of the Kinetics of Diffusion-Limited Reactions. *Phys. Rev.* **1957**, *107*, 463–470.
45. Mozer, A. J.; Dennler, G.; Sariciftci, N. S.; Westerling, M.; Pevrikas, A.; Osterbacka, R.; Juska, G. Time-Dependent Mobility and Recombination of the Photoinduced Charge Carriers in Conjugated Polymer/Fullerene Bulk Heterojunction Solar Cells. *Phys. Rev. B* **2005**, *72*, 035217(10).
46. Dennler, G.; Mozer, A. J.; Juska, G.; Pivrikas, A.; Osterbacka, R.; Fuchsbauer, A.; Sariciftci, N. S. Charge Carrier Mobility and Lifetime *versus* Composition of Conjugated Polymer/Fullerene Bulk-Heterojunction solar Cells. *Org. Electron.* **2006**, *7*, 229–234.
47. Pivrikas, A.; Sariciftci, N. S.; Juska, G.; Osterbacka, R. A Review of Charge Transport and Recombination in Polymer/Fullerene Organic Solar Cells. *Prog. Photovoltaicsc* **2007**, *15*, 677–696.
48. Hines, M.; Scholes, G. Colloidal PbS Nanocrystals with Size-Tunable Near-Infrared Emission: Observation of Post-Synthesis Self-Narrowing of the Particle Distribution. *Adv. Mater.* **2003**, *15*, 1844–1849.
49. Kang, M. S.; Lee, J.; Norris, D. J.; Frisbie, C. D. High Carrier Densities Achieved at Low Voltages in Ambipolar PbSe Nanocrystal Thin-Film Transistors. *Nano Lett.* **2009**, *9*, 3848–3852.
50. Kang, M. S.; Sahu, A.; Norris, D. J.; Frisbie, C. D. Size-Dependent Electrical Transport in CdSe Nanocrystal Thin Films. *Nano Lett.* **2010**, *10*, 3727–3732.
51. Barbour, L. W.; Pensack, R. D.; Hegadorn, M.; Arzhantsev, S.; Asbury, J. B. Excitation Transport and Charge Separation in an Organic Photovoltaic Material: Watching Excitations Diffuse to Interfaces. *J. Phys. Chem. C* **2008**, *112*, 3926–3934.
52. Pensack, R. D.; Banyas, K. M.; Barbour, L. W.; Hegadorn, M.; Asbury, J. B. Ultrafast Vibrational Spectroscopy of Charge Carrier Dynamics in Organic Photovoltaic Materials. *Phys. Chem. Chem. Phys.* **2009**, *11*, 2575–2591.
53. Pensack, R. D.; Banyas, K. M.; Asbury, J. B. Charge Trapping in Organic Photovoltaic Materials Examined with Time Resolved Vibrational Spectroscopy. *J. Phys. Chem. C* **2010**, *114*, 5344–5350.